RESEARCH LETTER

Key Points:

- Four segments of Quebrada transform system show significantly different seismic intensities
- One fracture zone segment appears to be seismogenic indicating local plate rotation
- Deep clouds of seismicity extend into the uppermost mantle at spreading center- transform fault intersections

Microseismicity Indicates Atypical Small-Scale Plate Rotation at the Quebrada Transform Fault System, East Pacific Rise

Jianhua Gong[1] , **Wenyuan Fan[1]** , and **Ross Parnell-Turner[1]**

[1]Scripps Institution of Oceanography, UC San Diego, La Jolla, CA, USA

Abstract Closely spaced, multi-strand ridge transform faults (RTFs) accommodate relative motions along fast spreading mid-ocean ridges. However, the relations between RTFs and plate spreading dynamics are poorly understood. The Quebrada system is one of the most unique RTF systems at the East Pacific Rise, consisting of four transform faults connected by three short intra-transform spreading centers (ITSCs). We use seven-months of ocean bottom seismograph data to study the Quebrada system, and find abundant earthquakes unevenly distributed among three active faults. We identify two deep, diffuse seismicity clouds at the inside corners of the ITSC-transform fault intersections, and one seismically active fracture zone. The observations suggest a complex regional plate-motion pattern, including possible heterogeneous rotations within the Quebrada system. Evolution of multi-strand RTFs may have resulted from a strong three-dimensional local thermal and fluid effects, while the RTFs may have also regulated regional tectonics, forming an intricate feedback system.

Plain Language Summary Mid-ocean ridge transform faults (RTFs) are plate boundaries that offset adjacent mid-ocean ridges. At fast spreading mid-ocean ridges, such as the East Pacific Rise (EPR), closely spaced, multi-strand RTFs are often connected by two or more short intra-transform spreading centers (ITSCs). However, physical processes accommodating plate spreading along such multi-strand RTF systems and the inter-relations between the fault system and the tectonic dynamics are not well understood. Quebrada is one of such multi-strand RTFs at the EPR. We utilize seven-month seismic data from ocean bottom seismographs of a 2008 experiment to investigate the seismotectonics of the region. We find intriguing, abundant seismicity on one of the fracture zones, contradicting the traditional view that fracture zones are seismically quiescent. Further, we identify two diffuse seismicity clouds penetrating the uppermost mantle at the inside corners of the ITSC-transform fault intersections, implying complex interactions among ITSCs, transform faults, and their surrounding structure. From these observations, we infer that there are rotational motions within the Quebrada fault system, which have caused slip along the fracture zone and facilitated fluid circulations to produce deep, diffuse seismicity. We speculate that there is a complex feedback system between the multi-strand RTFs and local three-dimensional tectonic processes.

1. Introduction

Mid-ocean ridge transform faults (RTFs) play a key role in plate tectonics, by offsetting spreading segments and thus accommodating relative motion between adjacent oceanic plates. These RTFs also form fracture zones, which are fossil fault traces located outside the inter-spreading regions, which are rarely reactivated except occasionally in close proximity to subduction zones (Contreras-Reyes & Carrizo, 2011; Hall et al., 2003; Lange et al., 2010; Robinson, 2011). The lengths of RTFs vary from ~30 to ~1,000 km (Bird, 2003), and most of the motion along RTFs is aseismic slip (Boettcher & Jordan, 2004; Boettcher & McGuire, 2009; Shi et al., 2021). Characteristic earthquakes (~M6) at RTFs show some of the most systematic and predictable rupture behaviors on Earth (McGuire, 2008; McGuire et al., 2012; Kuna et al., 2019). For example, M6 strike-slip earthquakes occur quasi-periodically every 5–6 years on the Gofar RTF in the equatorial East Pacific Rise (EPR), and it is thought that these earthquakes repeatedly break the same fault patches (McGuire et al., 2012). RTFs such as Gofar are well-documented, however most multi-strand RTFs, that is, those consisting of several transforms separated by small intra-transform spreading centers (ITSCs), are less well understood. Although multi-strand RTFs are fairly common along spreading centers such as the EPR, little is known about the relations between multi-strand RTFs and the thermal structure and tectonic processes at mid-ocean ridges (Fox & Gallo, 1984; Gregg et al., 2009; Morgan & Forsyth, 1988; Parmentier & Forsyth, 1985; Wolfson-Schwehr et al., 2017).

The Quebrada-Discovery-Gofar transform fault system on the EPR at ∼4°S includes eight ITSCs, which accommodate plate spreading at a half-rate of ∼70 mm/yr (Searle, 1983). The Gofar and Discovery systems have three and two fault segments bounding two and one ITSCs, respectively. The Quebrada fault system has four fault segments and three ITSCs. The Gofar and Discovery systems are comparable in size and kinematic setting, and both have physical features typical of a RTF system, including varying degrees of seismic coupling along strike, and frequent characteristic earthquakes (Guo et al., 2018; Kuna et al., 2019; McGuire et al., 2012; Wolfson-Schwehr et al., 2014). A one-year ocean bottom seismograph (OBS) deployment on the Gofar and Discovery faults identified seismic zones hosting regular M6 earthquakes, and aseismic zones primarily hosting microseismicity (Guo et al., 2018; McGuire et al., 2012). These observations suggest that slip can occur either fast or slowly on these faults, and that no portion of the segments is fully locked (Boettcher & Jordan, 2004; McGuire et al., 2012; Wolfson-Schwehr & Boettcher, 2019).

Despite being located only ∼37 km from the northern end of the Discovery fault segment, the seismicity and morphology of the Quebrada fault system differ from those of the Gofar and Discovery systems (Pickle et al., 2009). Between 1990 and 2008, only one $M > 5.5$ earthquake occurred in the Quebrada fault system (M5.6, 2003/12/19), while the Gofar and Discovery faults hosted 30 $M \geq 5.5$ earthquakes (Fox et al., 2001; McGuire, 2008). This contrasting seismogenic behavior suggests that different processes may be at play at Quebrada, and that its faulting configuration may be more complex than the idealized strike-slip motion as for other RTF systems. Here, we use seismic records from 11 OBSs to study the Quebrada transform system, which were part of a larger network, deployed to monitor seismicity across the whole Quebrada-Discovery-Gofar system from December 2007 to February 2009 (McGuire et al., 2012; Wolfson-Schwehr et al., 2014). We detect and locate earthquakes of the fault system and investigate the relations between the seismicity and regional tectonic processes. Our collective observations suggest that the seismicity may represent small-scale plate rotations and that multi-strand transform systems connected by short ITSCs may have played a role in modifying local thermal structure, fluid circulation, and melt migration in the vicinity of the transform system.

2. Quebrada Transform Fault System

The Quebrada transform fault system consists of four fault segments numbered Q1 to Q4 (north to south), extending 42, 24, 25, and 30 km, respectively (Figure 1). Fault strands have slightly varying orientation, with an average strike direction of ∼102°. The fault segments slip at a rate of ∼123–140 mm/yr (Searle, 1983; Wolfson-Schwehr & Boettcher, 2019), and the average fault zone width is about 2 km (Wolfson-Schwehr & Boettcher, 2019). These faults are separated by three ITSCs from north to south (numbered S9, S8, and S7, following convention of Pickle et al., 2009) with lengths of 4 km, 10 and 7 km, respectively. The across-axis extent of the volcanic terrain associated with individual ITSCs is difficult to define. The axial depths of each ITSC are 3.8–4.2 km, which is deeper than typical fast-spreading mid-ocean ridge segments, such as the one northeast of Q1, which is ∼3 km deep. There are several basins associated with S9, Q2, and S8—water depths are up to 4,600 m, and the water depth near S7 is ∼4,000 m. The Quebrada transform system is bounded by high relief flanks (north and south flanks in Figure 1) on both the north and south sides with a water depth range of 2500–3,000 m (Pickle et al., 2009). In contrast, the depths near S6 and EPR are about 3,200 m.

The Quebrada transform fault system has several unique geological and geophysical features, distinguishing itself from other typical RTFs. For example, residual mantle Bouguer anomalies of the region show that the deep basins around Q2 and S8 have crust only 3–4 km thick (Pickle et al., 2009). Further, the MgO content of rocks dredged from the three ITSCs indicate limited magmatic differentiation during crust generation, possibly due to relatively cool mantle temperatures and low magma supply (Pickle et al., 2009). The most perplexing attribute of the Quebrada fault system is the apparent lack of moderate magnitude (M > 5.5) events (McGuire, 2008). Only 73 $M \geq 3$ events that likely occurred in the system (in the region of 104°–102.5°W and 4.1°–3.45°S, Figure S1 in Supporting Information S1) were reported by International Seismological Centre (ISC) from 1 January 1980 to 1 January 2022 (International Seismological Centre, 2021). Given the fast half spreading rate (70 mm/yr) along the Quebrada transform fault, it is unclear how the plate motion is accommodated by the Quebrada faults without generating large magnitude events.

Plate motion and spreading processes regulate deformation between adjacent RTFs, and directly imprint on the morphology of spreading centers connecting these faults. For example, RTFs separated by tens of kilometers
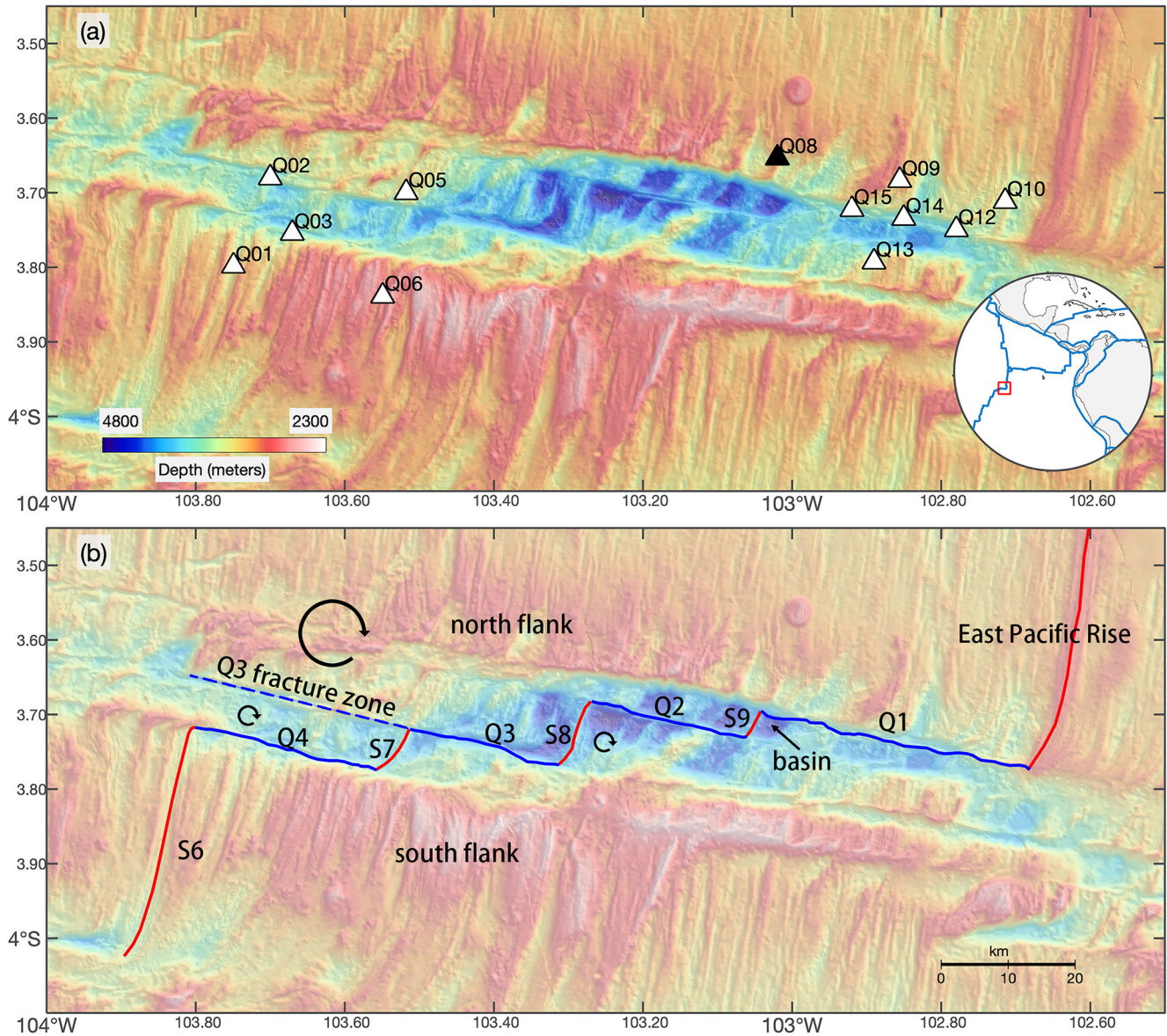
Figure 1. Bathymetry and structural interpretation of study area. (a) Bathymetry of study area. White labelled triangles are the 11 OBS stations that worked normally during the experiment. Station Q08 malfunctioned during the experiment. Inset shows location of study area at East Pacific Rise. (b) Structural interpretation of study area. Q1, Q2, Q3, and Q4 are surface traces of four segments of Quebrada transform system; S6, S7, S8, and S9 are ITSCs, following naming convention of Pickle et al. (2009); dashed line to the west of Q3 denotes Q3 fracture zone; basins and bathymetric highs (flanks) are also denoted on the maps. Circle arrows show the interpreted clock-wise rotation of the system.

are connected by mid-ocean ridges whose axial morphology closely correlates with the plate spreading rate (Macdonald, 1982; Smith & Sandwell, 1997). In contrast, more closely spaced, subparallel RTFs are commonly connected by step-overs, pull-apart basins, or narrow inter-transform spreading centers at fast spreading mid-ocean ridges, including the Quebrada transform fault system (Menard & Atwater, 1968; Searle, 1983; Wolfson-Schwehr & Boettcher, 2019). It is thought that the origins of such multi-strand RTFs is linked to changes in plate motion directions (Menard & Atwater, 1968; Pockalny et al., 1997). For instance, counter-clockwise spreading-direction rotation between the Pacific and Cocos plates in the past ~5 Myr has caused transtension along the left-lateral Siqueiros transform faults, and transpression along the right-lateral Clipperton transform fault (Gregg et al., 2009; Pockalny, 1997; Pockalny et al., 1997; Van Avendonk et al., 1998, 2001). Transpressional stress at Clipperton has generated median ridges along the fault, while transtensional stress at Siqueiros has caused extension within the system, leading to fissures and magma delivery to the seafloor, and forming a pull-apart basin or

ITSC. The rotation pattern is the opposite at the Quebrada-Discovery-Gofar system that all the transform faults are left-lateral, requiring a clock-wise rotation between the Pacific and Nazca plates.

3. Materials and Methods

3.1. Data

In 2008, an array of 30 broadband and 10 short-period three-component OBSs was deployed on the Quebrada-Discovery-Gofar transform fault system for a period of over 13 months (McGuire et al., 2012). Twelve of the instruments (four broadband and eight short-period stations) were free-fall deployed at the Quebrada transform system, although one station, Q08, did not record useful data (Figure 1). The network consisted of two 30 km aperture arrays, including seven OBSs on Q1 and five OBSs on Q4. The stations were located in water depths ranging from 3,300 to 3,870 m, and the OBSs recorded waveform data at a sampling rate of 100 Hz. The short period instruments' power supply was exhausted in July 2008 (Table S1), hence we only investigate the operational period from 1 January 2008 to 7 August 2008 (Julian Day 1–207) in this study. During the same time period, the ISC catalog reports two $M > 3$ events that occurred near the Quebrada transform system, both happening on 6 January 2008 (Table S2 in Supporting Information S1). Detailed data quality descriptions can be found in Text S1 in Supporting Information S1.

3.2. Earthquake Detection and Location

We apply a suite of techniques to detect, locate, and relocate earthquakes occurring on the Quebrada transform faults. We first detect seismic body wave arrivals of both P and S phases using a machine-learning phase picker, EQTransformer (Mousavi et al., 2020). EQTransformer is a deep-learning model for simultaneous earthquake detection and phase picking with uncertainty quantification. The method can detect P and S phases on single-station records for earthquakes occurring within a local distance, and the uncertainty of the phase picks are represented as confidence levels (probability). It is trained on a large-scale data set with 1 million earthquake records and 300 thousand noise waveforms (Mousavi et al., 2019). The earthquake waveforms of the training data set are mostly from events recorded within a few hundred kilometers. In contrast, earthquakes of the Quebrada faults are recorded by stations within tens of kilometers, which results in shorter S-P times. Therefore, we upsample the seismic records by a factor of two (200 Hz) to stretch the data before applying the EQTransformer detector. The procedure is similar to a strategy adopted by Wang et al. (2020) to detect earthquakes using dense nodal arrays. This approach extends the separation intervals for EQTransformer by assuming that records remain sampled at 100 Hz, and we later re-scale the detection time to its true sampling rate. Emergent P-waves are common in OBS data and could be challenging to pick by autopickers (e.g., McGuire et al., 2012). We find that EQTransformer can successfully detect emergent P-wave arrivals such as the example shown in Figure S20 in Supporting Information S1. However, this method can miss large magnitude events, such as the two $M > 3.5$ ISC events on 6 January 2008. Such events have very emergent P-arrivals and are challenging to identify even for experienced analysts (e.g., Figure S9 in Supporting Information S1). For these events, we manually pick the arrivals for subsequent location steps. In total, we detect ~390,000 P arrivals and ~420,000 S arrivals with an average confidence level of 0.5.

We then associate the obtained phase picks using an open-source algorithm, REAL (Zhang et al., 2019). REAL uses a grid-search method, and associates the phase picks and approximately locates a seismic event by counting the number of P and S picks and computing the travel-time residuals. A successful association must meet a predefined pick threshold within the predicted travel-time windows from a given velocity model (Zhang et al., 2019). In this study, we require a candidate earthquake having a minimum of 3 P arrivals and 4 total phase arrivals with a residual arrival time tolerance of 0.5 s. These requirements are relaxed comparing to typical onshore earthquake studies (e.g., Wang et al., 2020) to maximize detection with the sparse network at Quebrada. To ensure the location robustness, we apply further quality control procedures in later stages (described below). We use a 1D P-wave velocity profile extracted from a P-wave travel time tomographic model for the Quebrada system (Roland et al., 2012) for the association step (Figure S2 in Supporting Information S1). The velocity model approximates typical 2 Myr old oceanic crust and upper-mantle structure. We assume a constant Vp/Vs ratio of 1.9 for the crust (above 6.85 km depth) and 1.8 for the mantle (below 6.85 km depth) to obtain a 1D S-wave velocity model for this study. The grid-searching area covers a 0.2° radius region centering at the station that records the earliest phase

arrival and extends 20 km in depth. The searching grids are spaced 0.01° horizontally and 0.5 km vertically. In total, we identify 31,501 candidate earthquakes from the association step.

After making the phase associations, we use COMPLOC (Lin & Shearer, 2005, 2006) to invert the earthquake locations. The COMPLOC algorithm uses *P*- and *S*-wave arrival times to locate or relocate earthquakes. It applies a source-specific station term method to solve for local earthquake locations, which has the advantage of improving the relative location accuracy of nearby events by empirically correcting the effects of three-dimensional velocity structures (Lin & Shearer, 2005; Richards-Dinger & Shearer, 2000). The method is insensitive to phase-pick outliers as we select the ℓ_1 norm to evaluate the travel time residuals. Given the network configuration, some earthquakes are erroneously located to the seafloor. We have visually inspected some cases and conclude that these shallow earthquakes are likely mislocated. Therefore, we iteratively locate earthquakes with COMPLOC, and remove events placed within 1 km depth to the seafloor. We improve the earthquake locations by running this iterative procedure for 40 times (Figure S3 in Supporting Information S1), leading to 23,604 final, successful locations (Figure S4 in Supporting Information S1).

The earthquake locations are further refined using the GrowClust relocation method (Trugman & Shearer, 2017). The technique uses differential travel times obtained from cross correlations of *P* or *S* waveforms to determine the relative locations of event pairs at high precision. Similar relocation applications have proven crucial in revealing complex fault architectures and impulsive tectonic processes (Hauksson & Shearer, 2005; Parnell-Turner et al., 2017; Ross et al., 2019; Tan et al., 2016; Waldhauser & Ellsworth, 2000; Zhang & Thurber, 2003). The GrowClust algorithm is computationally efficient and can adaptively group events into clusters based on their waveform similarities. We only cross correlate *P* and *S* waves of the closest 100 events for each earthquake to obtain differential travel times. Such a selection procedure reduces the computational burden, and we successfully relocated 23,593 earthquakes in total (Figure 2).

To evaluate the robustness of the seismicity pattern, we select events with at least 4 *P* and 4 *S* picks and apply the same suite of techniques aforementioned. This exercise results in detecting, locating, and relocating ∼9,000 events (Figure S5 in Supporting Information S1). The results show similar earthquake distributions as of the full catalog, confirming the fidelity of our results. We further perform synthetic tests on the location results and assess the details in the Discussion.

3.3. Magnitude Calculation

We calculate local magnitude (M_L) of the earthquakes from 3-component displacement waveforms (Gutenberg & Richter, 1956). We first remove the instrument response and convolve the records with the Wood-Anderson instrument response. The waveforms are then filtered between 4 and 20 Hz and cut from 2 s before to 3 s after the *S* arrivals of an earthquake. The peak amplitude (*A*) is calculated as root sum square of the 3-component displacements. We also measure the peak noise amplitude (*N*) in the same way but using a window of 5–2 s before the *P* arrivals. We only keep a peak amplitude measurement if its signal-to-noise ratio (*A/N*) is greater than 10. The local magnitude is calculated as

$$M_L = \log_{10}(A) + 2.56\log_{10}(D) - 1.67, \tag{1}$$

where *D* is the hypocenter distance. A M_L is computed for each *S* phase measurement for a given event, and the final M_L of the earthquake is estimated as the median value of the population. To assure the robustness, an event is assigned a M_L only when there are more than three qualified *S* phase measurements. In total, we obtain M_L for 10,120 earthquakes. The magnitude-frequency distribution of the final catalog is shown in Figure S6 in Supporting Information S1, which follows a *b*-value close to 0.93 with a magnitude of completeness of 0.8.

4. Results

4.1. Seismicity Distribution

Earthquakes of the Quebrada system are unevenly distributed across the fault network with the majority of the seismicity occurring on Q4, Q3, and Q1 from west to east (Figure 2). Earthquakes on Q4 cluster into three distinct groups along the strike direction from −20 to 2 km at about 5 km depth, where the origin location coincides with the centroid of the earthquakes (3.764°S/103.615°W, Figures 2c and 2d). These earthquakes form a strike
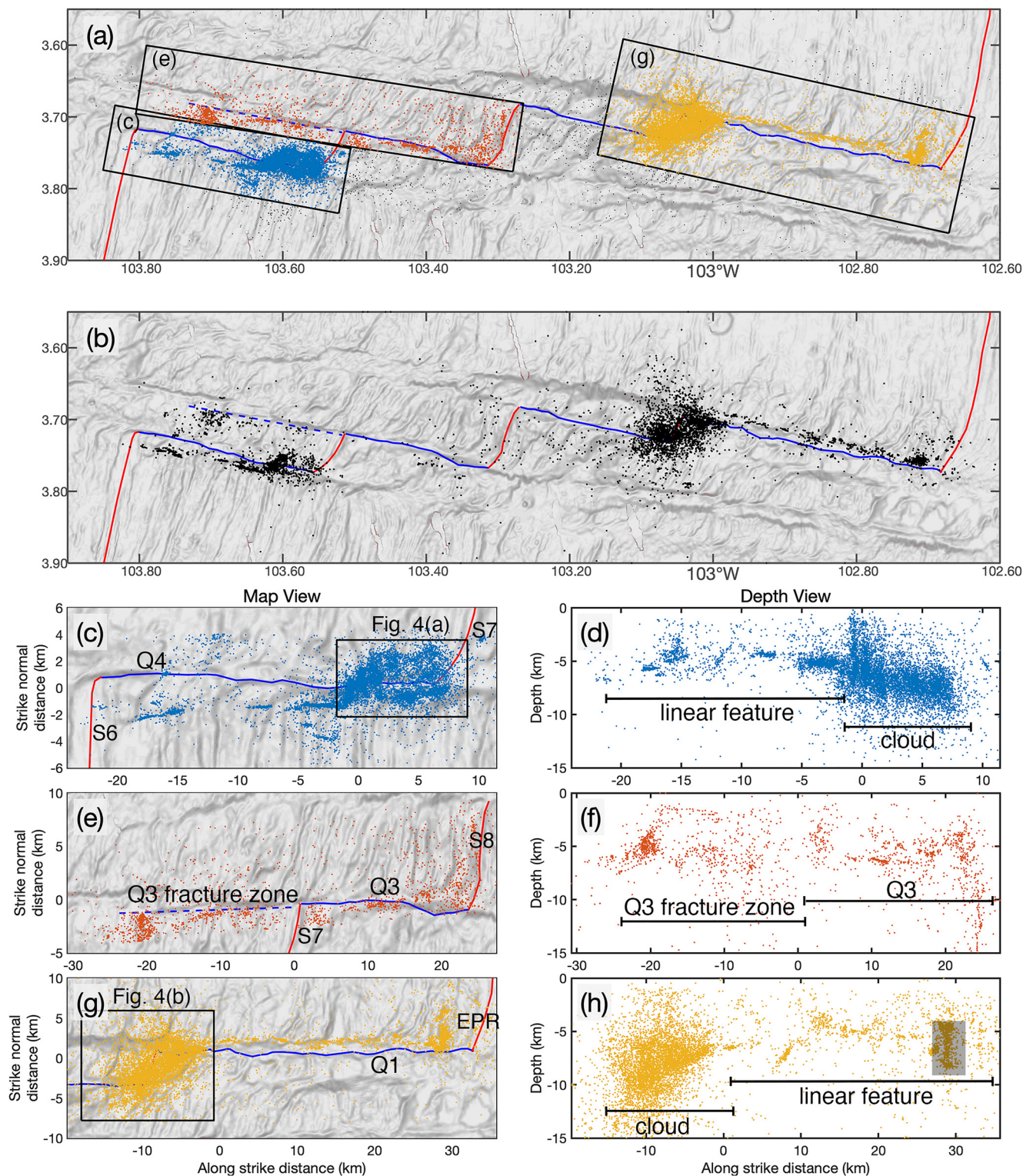
Figure 2. Earthquake hypocenters. (a) Map view of earthquake locations from the full catalog, with shaded relief background. Three rectangular boxes denote the subset of events on Q4, Q3, and Q1, respectively. Blue, red and blue dashed lines are surface traces of transform faults, ITSCs and Q3 fracture zone, respectively. (b) Map view of earthquake locations for events with more than 4 *P*- and 4 *S*-picks. (c–h) Zoom-in map and depth profiles of seismicity on faults Q4, Q3, and Q1. Blue lines denote transform fault surface traces. Blue dashed line denotes Q3 fracture zone. Red lines denote ITSCs and EPR. The two boxes in (c and g) highlight the two clouds of seismicity at the inside corners of the ridge-transform intersections (Figure 4). Gray shaded region in (h) indicates where earthquake locations are more uncertain.

parallel strand that is south of the surface fault trace, indicating a non-vertical fault plane dipping at 68° towards the south. There is a diffuse seismicity cloud locating in between −2 and 8 km along strike that is west of the ITSC S7. This cloud occupies the inner corner of the ridge-transform intersection (Q4-S7), but does not extend beyond eastern S7.

There are fewer earthquakes on Q3 compared to those on Q4. However, seismicity on Q3 aligns well with the bathymetric fabric, indicating a near-vertical fault plane (Figures 2e and 2f). Intriguingly, a band of ∼1,000 earthquakes extends ∼25 km west beyond the actively slipping portion of Q3, presumably trending along an abandoned fault segment of Q3 (i.e., the fracture zone; Figure 2e). These observations challenge the conventional assumption that there is no relative motion along fracture zones in such RTF systems. In order to better visualize this configuration, we use a local coordinate system to plot seismicity with origin at 3.715°S/103.520°W. A cluster of events spread a spatial footprint of ∼3 km at −20 km along the strike direction and at 5 km depth (Figures 2e and 2f), which marks the edge of the detected earthquakes on the Q3 fault strand. We also observe some possible deep events along ITSC S8. We confirm the location of these earthquakes by performing a synthetic test as detailed below. Locations of these events are, however, relatively more uncertain than others in the catalog, because they are located 50 km from the two OBS arrays (Figures 1 and 2). Few earthquakes were identified along Q2, which could indicate a seismically quiescent fault strand, or, given the network configuration, could just be due our limited ability to resolve seismicity there.

Seismicity on Q1 shares resemblance with earthquakes on Q4. By projecting the earthquakes into a local coordinate with the origin at the centroid of the seismicity (3.720°S/102.972°W), we identify one group of earthquakes situated between 0 and 28 km that define a linear trend. This strand of earthquakes deviates away from the seafloor fault trace, suggesting a fault plane dipping ∼80° towards the north (Figures 2g and 2h). Another diffuse group of earthquakes is located between −12 and 0 km along the strike direction. The diffuse pattern of these earthquakes is similar to those of Q4 reaching a deep depth up to 15 km towards the west. This cluster of earthquakes trends along an oblique direction east of ITSC S9 in the inner corner of the ridge-transform intersection (S9-Q1). There is an apparent group of earthquakes forming a strike-normal feature near ∼30 km along the strike direction (shaded area in Figure 2h). However, this feature is not present in the catalog requiring events having at least 4 P and 4 S picks, suggesting its large uncertainties (Figure 2b; Figure S5 in Supporting Information S1).

4.2. Spatiotemporal Earthquake Clusters

Seismicity seems to progress in space and time differently between the different Quebrada fault segments (Figure 3). To identify and analyze possible clusters of earthquakes, we first project the hypocenters into a 2D space-time domain with the space domain parallel to the mean fault strike direction (102°) and the time domain defined as Julian day of 2008. We then define earthquake clusters as those falling within a neighborhood-search radius of 1.3 and a minimum number of neighbors of 40 events using a density based clustering algorithm (e.g., function dbscan, MATLAB, 2018). Events not meeting this criterion for clustering are assumed to be isolated events (Ester et al., 1996). In order to test the sensitivity of our clustering approach to these parameters, we varied different parameter combinations, as given in Table S3 in Supporting Information S1. In general, larger neighborhood-searching radius and smaller minimum number of neighbors results in a greater number of (smaller) clusters. The preferred parameters here are determined by a trial and error approach, which balances the number and density of the clusters (Figure 3). This exercise recognizes several clusters on Q1, Q3, and Q4, and they are color coded by their occurrence time in Figure 3. The spatial centroids of each cluster are shown in Figure 4.

Along Q4, all the identified clusters are located within the seismicity cloud near the ridge-transform intersection. The seismicity cloud can be roughly divided into two subareas: a western part with some vertical-trending seismicity and an eastern part with more diffuse seismicity (Figure 4; Figure S7 in Supporting Information S1). The western portion is connected to the Q4 transform fault by a band of linear seismicity at ∼5 km depth (Figure 4a). Events in this western sub-area are distributed from the seafloor to depths of 5 km, while seismicity extends deeper from ∼5–8 km as for the eastern subarea. In total, 12 clusters are identified within the Q4 seismicity cloud. Seven clusters were located in the western end of Q4, and five clusters were located in the eastern portion of Q4 (Figure S8 in Supporting Information S1). Cluster 1 is the largest cluster and is related to the increase in seismicity rate for about 20 days at the beginning of 2008 (Figure 4d).
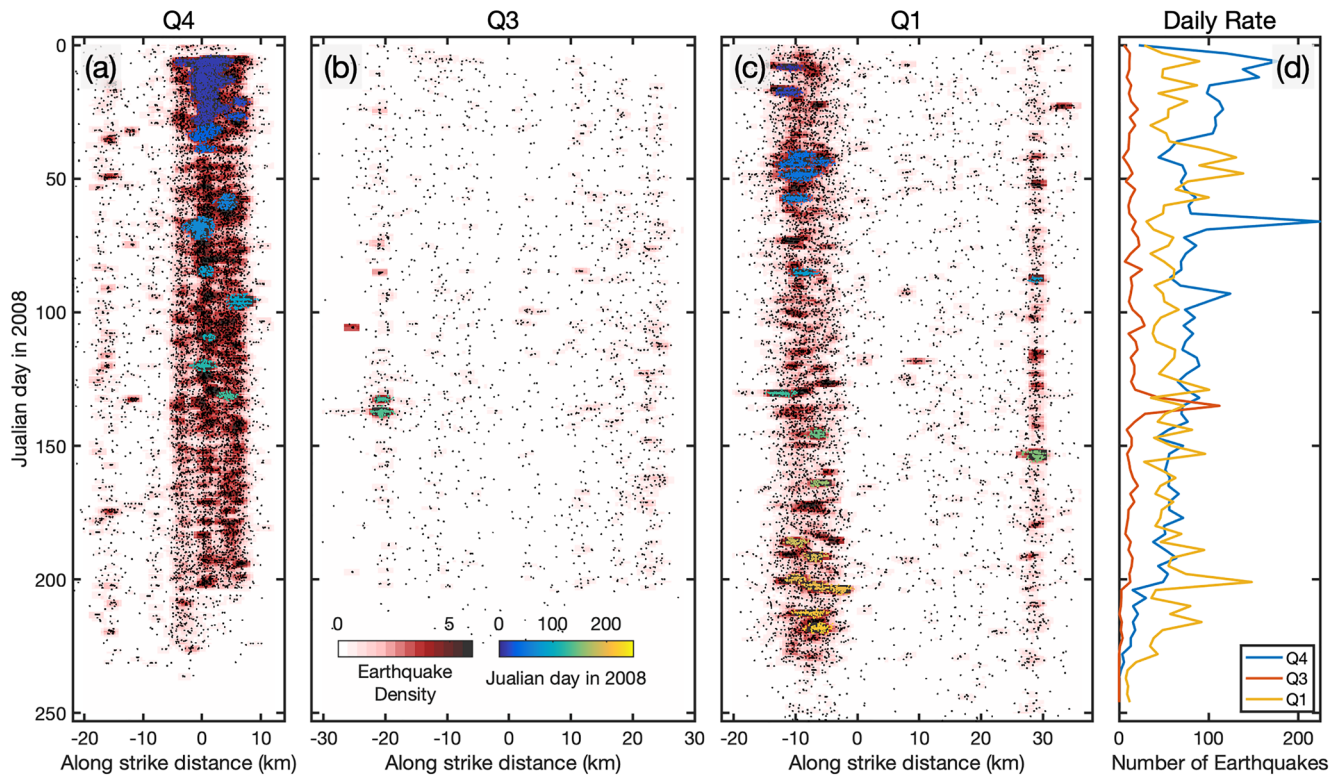
Figure 3. Spatiotemporal evolution of the Quebrada microearthquakes. (a–c) Spatiotemporal evolution of seismicity on Q4, Q3, and Q1 in the three rectangular boxes in Figure 2, respectively. Black dots are earthquakes plotted on top of a red scale earthquake density plot. Colored zones are clusters identified along each fault segment. (d) Daily seismicity rates of Q4, Q3, and Q1 that are summed over every 2 days.
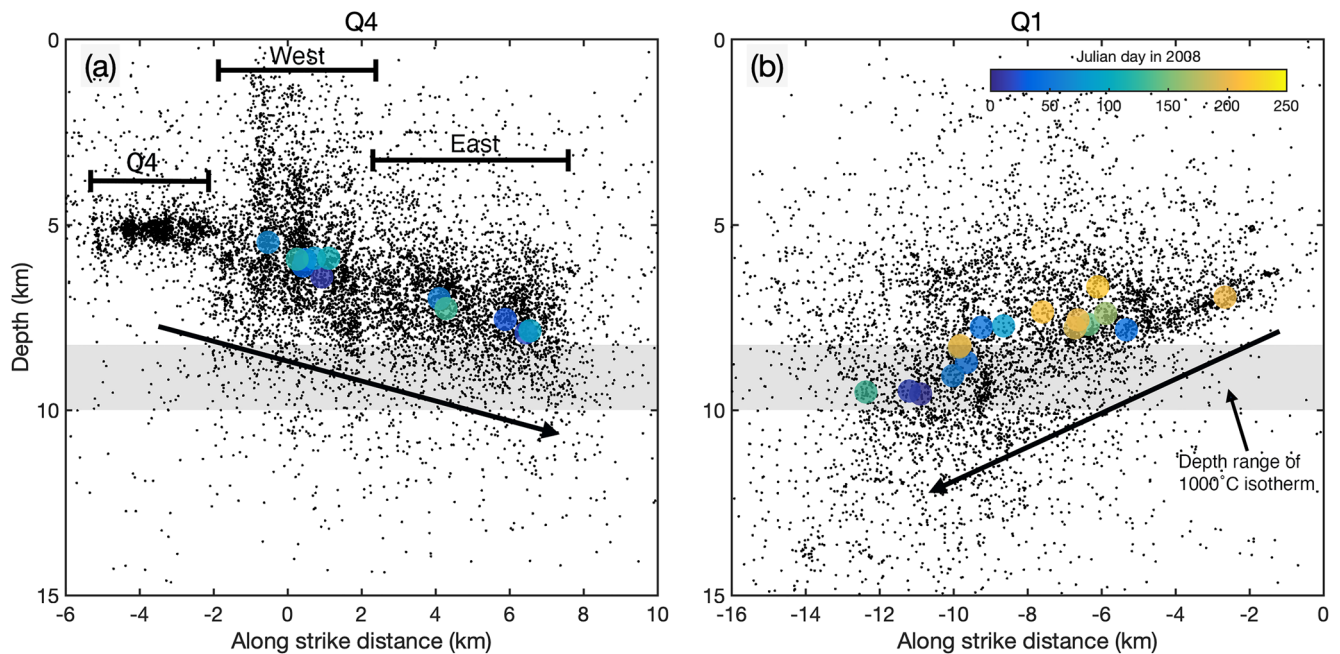

Figure 4. Depth profiles through two seismicity clouds in Figure 2 and the centroid locations of clusters in Figure 3. (a) Q4 seismicity cloud and (b) Q1 seismicity cloud. Black dots show earthquakes. Filled colored circles denote the centroids of seismicity clusters. Black bars in (a) indicate the seismicity that are associated with Q4 transform faults, and the west and the east parts of the Q4 seismicity cloud. Black arrows in (a) and (b) denote the inferred dipping directions of the seismicity clouds. The transparent gray bands show a depth range (8–10 km) of 1,000°C isotherm for the ambient mantle at the Quebrada system from Pickle et al. (2009).

Seismicity abruptly progressed along Q4 around Julian day 6 (Figure 3d). This change might have been triggered by two $M \geq 3$ events on 6 January 2008 (Table S2 in Supporting Information S1, Event 1 and 2). We located these two events with a grid-search method using manually picked P-wave arrivals (Text S2 in Supporting Information S1), and their locations are within the Q4 cloud as shown in Figure S9 in Supporting Information S1. Events 1 and 2 are both located in the western part of the Q4 seismicity cloud, with event 1 located at ~8 km depth to the east and event 2 to the west with its depth unresolved (Table S2 in Supporting Information S1). The event 1–2 sequence shows a clear migration pattern from east to west at a speed of ~0.8 km/hr (Figure S10 in Supporting Information S1).

Two clusters are identified on the Q3 fracture zone around day 135 (Figure 3b). The two clusters locate at about −20 km along the strike direction and at a depth of about 5 km (Figures 2e and 2f). They correspond to the highest seismicity rate along Q3 during the experiment (Figure 3d).

For Q1, we identified 17 temporal clusters in the diffuse cloud (Figure 4; Figure S11 in Supporting Information S1). The Q1 cloud has an apparent westward dipping feature towards the ITSC S9. However, there are no clear linear trending features in these clusters. The 17 clusters span across the whole diffuse cloud. Three clusters occurred on day 199, 202, and 203 are likely migrating sequences of events propagating from west to east, connecting the diffuse cloud to the transform fault Q1.

5. Discussion

5.1. Location Uncertainty

We evaluate the robustness of our hypocenter location estimates by performing synthetic resolvability experiments in the Q1 and Q4 diffuse clouds, and on the apparently abandoned fault segment of Q3. We use our final relocation results as input to generate synthetic P and S arrival times using the same 1D velocity model used in the location procedure. For a given case, the synthetic arrival times are only computed for stations that were used to locate the observed event. We further explore uncertainty by adding random, normally distributed errors to the synthetic arrival times. We assume the distributions have zero means but have independent standard deviations (σ) for P and S arrival times. We test three pairs of σ for the P and S arrival times as listed in Table S4 in Supporting Information S1. These values represent realistic picking errors as they are adopted from the training data set of the EQTransformer algorithm (Mousavi et al., 2020). In total, we construct four sets of synthetic datasets, including one without random errors, and apply the COMPLOC algorithm to these arrival times to invert for earthquake locations (Lin & Shearer, 2005, 2006).

We find the major tectonic trends defined by the hypocenters can be fully recovered for all four trial datasets. Epicentral location differences (i.e., latitude and longitude) between the synthetic and observed locations are generally less than 0.04° (>99%, Figures S12–S13 in Supporting Information S1). Location differences for Q3 earthquakes that are on the active fracture zone segment are less than 0.01° (>99%, Figure S13b in Supporting Information S1). Hypocenter depth can be reliably resolved since the majority of earthquakes in the deep diffuse clouds are consistently located at depths of 5–10 km (Figure S14 in Supporting Information S1). Three-dimensional velocity variations can also cause location biases, but are unlikely to distort the observed features because of the relatively homogeneous velocity structures of the region (Roland et al., 2012). Clock drift of the OBSs could be another source of location errors (Gouédard et al., 2014), but such an effect is corrected by the instrument center and we do not observe clear differences in earthquake locations during the experiment period.

We note that the synthetic tests do not explore the true location uncertainties but only show that the key features can be recovered by the network configuration, and hence our tests likely represent a best case scenario. Therefore, we examine events with more than four P arrival picks and more than four S arrival picks, and only interpret features that are robustly resolved for this superior quality catalog (Figure S5 in Supporting Information S1). The major features discussed in Section 4 are also observed in this catalog (Figure S5 in Supporting Information S1), showing similar key features as for the whole catalog. In particular, seismicity on the Q3 fracture zone and in the two deep diffuse clouds are also located at similar locations as those in the full catalog (Figure S5 in Supporting Information S1). To further evaluate the diffuse cloud features at Q1 and Q4, we examine the cross correlation results from our relocation procedure and also further pair-wise cross correlate all the events in the same cloud. The cross correlation results suggest limited similarities of the P or S waveforms (low cross correlation coefficients),

indicating these earthquakes were unlikely from the same positions with the same focal mechanisms. Based on these tests, the reported features in the study are likely real.

5.2. Seismicity and Slip Along Transform Faults

Except for the earthquakes in the two deep diffuse clouds, most of the microearthquakes that occurred on Q4, Q3, and Q1 are at a depth around 5 km, defining linear features oriented parallel to surface fault traces (Figure 2). The lack of earthquakes for fault patches shallower than 5 km depth seems to suggest that these fault patches are partially locked and greater earthquakes may occur there occasionally. However, the network configuration may have limited location resolution for shallower earthquakes, leaving the physical nature of the shallow fault patches uncertain. At Quebrada, the sharp contrast between the fast spreading rate (∼123 mm/yr) and a lack a moderate magnitude earthquakes (only 73 $M > 3$ events since 1980) suggests that most of the plate spreading may have been accommodated by aseismic slip along these Quebrada faults. RTF segments that are dominated by aseismic slip, however, tend to have active microearthquakes that can extend into the uppermost mantle (McGuire et al., 2012). Such segments may have experienced higher degrees of damage compared to more intact patches that can host M6 earthquakes, such as the barrier zones of the Gofar and Discovery systems (McGuire et al., 2012; Wolfson-Schwehr et al., 2014). There are no such barrier zones observed in the Quebrada system. These apparent contrasts between Quebrada and other RTF systems are not consistent with current understanding of deformation partitioning at oceanic transform faults.

We observe few events on the Q2 fault, which could be due to the observational limit as our stations are away from the fault strand. Alternatively, the possible lack of seismicity could indicate that most of the displacement along Q2 is accommodated by aseismic slip, which may have resulted from the unusually thin crust (3–4 km) there in the deep basins (Pickle et al., 2009). This relatively thin crust could lead to a fault damage zone with a limited depth extent, and the deep basins might have been undergoing extension, which would cause a low normal stress on the Q2 segment. The combination of the two effects would favor aseismic slip, rather release of accumulated strain via large earthquakes (Liu et al., 2012; Liu & Rice, 2005). Such an interpretation can explain that a 17-year earthquake catalog on Quebrada detected much fewer events along Q2 than on other three segments, and there are no $M > 5.5$ events found on Q2 segment either (McGuire, 2008). We further speculate that the deformation mechanisms controlling Q2 and other Quebrada faults are likely different, given the varying seismicity and possibly distinct crustal structures.

Surprisingly, we observe abundant seismicity on the fracture zone segment of the Q3 transform fault, which contradicts the conventional idea that no relative slip occurs along fracture zones (Bondár & Storchak, 2011; Engdahl et al., 1998; Tucholke & Schouten, 1988). The presence of these earthquakes suggests relative motion on either side of the Q3 fracture zone, and the strike of Q3 (98°) is different from those of Q1 and Q4 (102°; Figure S15 in Supporting Information S1). These combined observations could be explained by a local rotation within the Quebrada system. This rotation is consistent with the suggested clockwise change in rotation of the plate spreading direction between the Pacific and Nazca plates over the past few million years (Lonsdale, 1989). The clockwise rotation in plate spreading direction is inferred from the trend of several multi-strand transform systems in the southern EPR (Lonsdale, 1989), and is hence tentative. Nonetheless, S9 is the youngest and shortest ITSC (4 km) among the Quebrada spreading centers (Pickle et al., 2009), meaning that accommodating this change in spreading direction may be easier there than on other ITSCs in the system. Hence the Q3 fault could be undergoing clockwise rotation in order to reach equilibrium with the current spreading direction, which could explain the observed seismicity on the Q3 fracture zone.

5.3. Diffuse Seismicity

One of the most striking features of the Quebrada catalog presented here is the pair of diffuse clouds of seismicity at the inside corners of the ridge-transform intersections at Q1-S9 and Q4-R7. These earthquakes form two dipping trends, which deepen towards the ITSCs, with earthquakes mostly located at depths of 5–10 km. These earthquakes are considerably deeper than other events in the region (Figure 4). A regional three-dimensional thermal model shows that the Quebrada area is relatively cooler than the neighboring Discovery-Gofar system, and predicts that the depth of 1,000°C isotherm is 8–10 km at Quebrada (Pickle et al., 2009). Since earthquakes in the two diffuse zones are observed within this depth window, which is beyond the typical frictional stability

transition at ~500°–600°C (Boettcher et al., 2007; He et al., 2007), additional mechanisms, not included in the thermal model, are likely required to explain the deep seismicity.

Two diffuse clouds co-locate within the deep basins, and we infer that the same extensional processes that have formed the basins may also explain the origin of these earthquakes. In conjunction with the possibility of small-scale rotation, transtension could create damage zones at the inside corners of the ridge-transform intersections. Because of the continuous rotation, these damage zones could lead to enhanced permeability, and promote enhanced fluid circulation through the crust and upper mantle, and thus lower ambient temperatures (Grevemeyer et al., 2019; Schlindwein, 2020; Schlindwein & Schmid, 2016). Such processes may favor the generation of serpentine, talc, or other altered mineral phases in the upper mantle, leading to heterogeneous stress conditions and distributed seismicity. This distributed pattern of alteration and deformation could explain the observed clusters in the two deep clouds, the apparent lack of systematic migration patterns in the clouds, and bursts of seismicity which could be driven by localized episodes of fluid circulation (Figure 4; Figures S8 and S11 in Supporting Information S1).

Alternatively, the presence of high-temperature fractures under high temperature conditions in the semiductile mylonites (Yu et al., 2021) or coarse-grained peridotite can also sustain brittle behaviour at greater pressure-temperature conditions (Kohli et al., 2021). Such processes could have facilitated the observed deep seismicity at 8–10 km depth without significant reduction in the mantle temperatures. For example, deep fluid-rock interaction, weakening and strain localization within the oceanic lithosphere beneath transform faults can cause brittle fracture at temperatures over 800°C (Prigent et al., 2020). In all possible scenarios, fluids likely have played an important role in generating the deep, diffuse seismicity. The small-scale rotation and extension at the transform fault and ITSC intersections might have created fluid circulation pathways and further facilitated the interaction between fluid and oceanic lithosphere.

The deepening trend of the two seismicity clouds towards ITSCs might relate to melt migration and/or faulting induced enhanced hydrothermal circulation. Models of three-dimensional melt flow at segmented transform systems show that melt associated with relatively short ITSCs is likely to migrate towards adjacent, longer spreading segments (Gregg et al., 2009). In this model, depth to the top of the melt is deeper at the ITSC and shallower at the adjacent mid-ocean ridge, sharing a similar geometry as the dipping structure of the seismicity clouds observed at Quebrada. If a comparable melt flow regime applies to the Quebrada system, the intense seismicity clouds might reflect an ongoing extraction of melt at the ITSCs towards the adjacent spreading segments. However, the causality between the melt migration and intense seismicity at the ridge-transform intersection is unclear. For example, the melt migration and seismicity distribution might both be by-products of other physical mechanisms, such as the three-dimensional thermal and stress redistribution due to the ridge-transform intersection. Faulting process due to temporally discontinuous or spatially heterogeneous rotation could be another explanation for the observed seismicity. Although the earthquake clouds have a diffuse rather than planer geometry, they might represent an earlier stage of the opening of the pull-apart basin, due to the rotation of the Quebrada fault system in response to the current plate spreading direction. Furthermore, the Q4 diffuse cloud is moderately more focused than that of Q1, which is consistent with the inference that S9 is the most recently developed ITSC in the Quebrada transform system (Pickle et al., 2009). The two diffuse clouds are located in the inside corners of the spreading center and transform fault intersections, which indicates possible differences between the two sides of the ITSCs in terms of stress state, fluid circulation, melt supply, and material properties.

6. Conclusions

We use seven months of OBS data to detect and locate 23,593 earthquakes on multiple strands of the Quebrada transform fault system. Three of the four transform faults (Q1, Q3, and Q4) are seismically active, while the other fault segment (Q2) likely slips aseismically. We find abundant seismicity along the (supposedly inactive) Q3 fracture zone, and a pair of diffuse seismicity clouds associated with transform faults Q1 and Q4. These two clouds are at the inside corners of the intersections between the ITSCs and the transform faults, extend into the uppermost mantle (5–10 km), and deepen towards the ITSCs. We infer that brittle deformation associated with these deep clouds is related to enhance fluid circulation down to upper mantle that might have lowered the mantle temperature or weakened the oceanic lithosphere through fluid-rock interactions. Such effects may relate to heterogeneous rotational motions within the Quebrada system, which could explain the active abandoned fault

of Q3. We speculate that the tectonic processes and displacement on these multi-strand transform faults likely experience positive feedbacks, and that atypical earthquakes are caused by local small-scale rotations in response to regional changes in plate spreading direction.

Data Availability Statement

The seismic data are available from the Data Management Center (DMC) of the Incorporated Research Institutions for Seismology (IRIS) under the network codes ZD. IRIS Data Services, and the IRIS Data Management Center, were used to access waveforms, related metadata, and derived products used in this study. The earthquake catalog was downloaded from the International Seismological Center (ISC) and the bathymetry data can be obtained from https://www.ngdc.noaa.gov/maps/autogrid/. We used open-source software EQTransformer (Mousavi et al., 2020), REAL (Zhang et al., 2019), COMPLOC (Lin & Shearer, 2006) and GrowClust (Trugman & Shearer, 2017) for earthquake detection, association, location and relocation. The earthquake catalog is included in the supplementary material and is also archived at Marine Geoscience Data System, Cruise DOI: https://doi.org/10.26022/IEDA/330427 (http://get.iedadata.org/doi/330427).

References

Bird, P. (2003). An updated digital model of plate boundaries. *Geochemistry, Geophysics, Geosystems*, *4*(3). https://doi.org/10.1029/2001GC000252

Boettcher, M. S., Hirth, G., & Evans, B. (2007). Olivine friction at the base of oceanic seismogenic zones. *Journal of Geophysical Research*, *112*(B1). https://doi.org/10.1029/2006jb004301

Boettcher, M. S., & Jordan, T. H. (2004). Earthquake scaling relations for mid-ocean ridge transform faults. *Journal of Geophysical Research*, *109*(B12). https://doi.org/10.1029/2004JB003110

Boettcher, M. S., & McGuire, J. J. (2009). Scaling relations for seismic cycles on mid-ocean ridge transform faults. *Geophysical Research Letters*, *36*(21). https://doi.org/10.1029/2009GL040115

Bondár, I., & Storchak, D. (2011). Improved location procedures at the international seismological centre. *Geophysical Journal International*, *186*(3), 1220–1244. https://doi.org/10.1111/j.1365-246X.2011.05107.x

Contreras-Reyes, E., & Carrizo, D. (2011). Control of high oceanic features and subduction channel on earthquake ruptures along the Chile–Peru subduction zone. *Physics of the Earth and Planetary Interiors*, *186*(1), 49–58. https://doi.org/10.1016/j.pepi.2011.03.002

Engdahl, E. R., van der Hilst, R., & Buland, R. (1998). Global teleseismic earthquake relocation with improved travel times and procedures for depth determination. *Bulletin of the Seismological Society of America*, *88*(3), 722–743. https://doi.org/10.1785/BSSA0880030722

Ester, M., Kriegel, H., Sander, J., & Xu, X. (1996). A density-based algorithm for discovering clusters in large spatial databases with noise. In *Proceedings of the second international conference on knowledge discovery in databases and data mining* (pp. 226–231). AAAI Press.

Fox, C. G., Matsumoto, H., & Lau, T.-K. A. (2001). Monitoring Pacific Ocean seismicity from an autonomous hydrophone array. *Journal of Geophysical Research*, *106*(B3), 4183–4206. https://doi.org/10.1029/2000JB900404

Fox, P. J., & Gallo, D. G. (1984). A tectonic model for ridge-transform-ridge plate boundaries: Implications for the structure of oceanic lithosphere. *Tectonophysics*, *104*(3), 205–242. https://doi.org/10.1016/0040-1951(84)90124-0

Gouédard, P., Seher, T., McGuire, J. J., Collins, J. A., & van der Hilst, R. D. (2014). Correction of ocean-bottom seismometer instrumental clock errors using ambient seismic noise. *Bulletin of the Seismological Society of America*, *104*(3), 1276–1288. https://doi.org/10.1785/0120130157

Gregg, P. M., Behn, M. D., Lin, J., & Grove, T. L. (2009). Melt generation, crystallization, and extraction beneath segmented oceanic transform faults. *Journal of Geophysical Research*, *114*(B11). https://doi.org/10.1029/2008JB006100

Grevemeyer, I., Hayman, N. W., Lange, D., Peirce, C., Papenberg, C., Van Avendonk, H. J., et al. (2019). Constraining the maximum depth of brittle deformation at slow- and ultraslow-spreading ridges using microseismicity. *Geology*, *47*(11), 1069–1073. https://doi.org/10.1130/G46577.1

Guo, H., Zhang, H., & Froment, B. (2018). Structural control on earthquake behaviors revealed by high-resolution Vp/Vs imaging along the Gofar transform fault, East Pacific Rise. *Earth and Planetary Science Letters*, *499*, 243–255. https://doi.org/10.1016/j.epsl.2018.07.037

Gutenberg, B., & Richter, C. F. (1956). Earthquake magnitude, intensity, energy, and acceleration: (Second paper). *Bulletin of the Seismological Society of America*, *46*(2), 105–145. https://doi.org/10.1785/BSSA0460020105

Hall, C. E., Gurnis, M., Sdrolias, M., Lavier, L. L., & Müller, R. (2003). Catastrophic initiation of subduction following forced convergence across fracture zones. *Earth and Planetary Science Letters*, *212*(1), 15–30. https://doi.org/10.1016/S0012-821X(03)00242-5

Hauksson, E., & Shearer, P. (2005). Southern California hypocenter relocation with waveform cross-correlation, Part 1: Results using the double-difference method. *Bulletin of the Seismological Society of America*, *95*(3), 896–903. https://doi.org/10.1785/0120040167

He, C., Wang, Z., & Yao, W. (2007). Frictional sliding of gabbro gouge under hydrothermal conditions. *Tectonophysics*, *445*(3–4), 353–362. https://doi.org/10.1016/j.tecto.2007.09.008

International Seismological Centre. (2021). *On-line bulletin*.

Kohli, A., Wolfson-Schwehr, M., Prigent, C., & Warren, J. M. (2021). Oceanic transform fault seismicity and slip mode influenced by seawater infiltration. *Nature Geoscience*, *14*(8), 606–611. https://doi.org/10.1038/s41561-021-00778-1

Kuna, V. M., Nábělek, J. L., & Braunmiller, J. (2019). Mode of slip and crust–mantle interaction at oceanic transform faults. *Nature Geoscience*, *12*(2), 138–142. https://doi.org/10.1038/s41561-018-0287-1

Lange, D., Tilmann, F., Rietbrock, A., Collings, R., Natawidjaja, D. H., Suwargadi, B. W., et al. (2010). The fine structure of the subducted Investigator Fracture Zone in western Sumatra as seen by local seismicity. *Earth and Planetary Science Letters*, *298*(1), 47–56. https://doi.org/10.1016/j.epsl.2010.07.020

Lin, G., & Shearer, P. (2005). Tests of relative earthquake location techniques using synthetic data. *Journal of Geophysical Research*, *110*(B4). https://doi.org/10.1029/2004JB003380

Lin, G., & Shearer, P. (2006). The COMPLOC earthquake location package. *Seismological Research Letters*, *77*(4), 440–444. https://doi.org/10.1785/gssrl.77.4.440

Liu, Y., McGuire, J. J., & Behn, M. D. (2012). Frictional behavior of oceanic transform faults and its influence on earthquake characteristics. *Journal of Geophysical Research*, *117*(B4). https://doi.org/10.1029/2011JB009025

Liu, Y., & Rice, J. R. (2005). Aseismic slip transients emerge spontaneously in three-dimensional rate and state modeling of subduction earthquake sequences. *Journal of Geophysical Research*, *110*(B8). https://doi.org/10.1029/2004JB003424

Lonsdale, P. (1989). Segmentation of the Pacific-Nazca spreading center, 1°N–20°S. *Journal of Geophysical Research*, *94*(B9), 12197–12225. https://doi.org/10.1029/JB094iB09p12197

Macdonald, K. C. (1982). Mid-ocean ridges: Fine scale tectonic, volcanic and hydrothermal processes within the plate boundary zone. *Annual Review of Earth and Planetary Sciences*, *10*(1), 155–190. https://doi.org/10.1146/annurev.ea.10.050182.001103

MATLAB. (2018). *9.7.0.1190202 (r2019b)*. Natick, MA: The MathWorks Inc.

McGuire, J. J. (2008). Seismic cycles and earthquake predictability on East Pacific Rise transform faults. *Bulletin of the Seismological Society of America*, *98*(3), 1067–1084. https://doi.org/10.1785/0120070154

McGuire, J. J., Collins, J. A., Gouédard, P., Roland, E., Lizarralde, D., Boettcher, M. S., et al. (2012). Variations in earthquake rupture properties along the Gofar transform fault, East Pacific Rise. *Nature Geoscience*, *5*(5), 336–341. https://doi.org/10.1038/ngeo1454

Menard, H. W., & Atwater, T. (1968). Changes in direction of sea floor spreading. *Nature*, *219*(5153), 463–467. https://doi.org/10.1038/219463a0

Morgan, J. P., & Forsyth, D. W. (1988). Three-dimensional flow and temperature perturbations due to a transform offset: Effects on oceanic crustal and upper mantle structure. *Journal of Geophysical Research*, *93*(B4), 2955–2966. https://doi.org/10.1029/JB093iB04p02955

Mousavi, S. M., Ellsworth, W. L., Zhu, W., Chuang, L. Y., & Beroza, G. C. (2020). Earthquake transformer—An attentive deep-learning model for simultaneous earthquake detection and phase picking. *Nature Communications*, *11*(1), 3952. https://doi.org/10.1038/s41467-020-17591-w

Mousavi, S. M., Sheng, Y., Zhu, W., & Beroza, G. C. (2019). STanford EArthquake Dataset (STEAD): A global data set of seismic signals for AI. *IEEE Access*, *7*, 179464–179476. https://doi.org/10.1109/ACCESS.2019.2947848

Parmentier, E. M., & Forsyth, D. W. (1985). Three-dimensional flow beneath a slow spreading ridge axis: A dynamic contribution to the deepening of the median valley toward fracture zones. *Journal of Geophysical Research*, *90*(B1), 678–684. https://doi.org/10.1029/JB090iB01p00678

Parnell-Turner, R., Sohn, R., Peirce, C., Reston, T., MacLeod, C., Searle, R., & Simão, N. (2017). Oceanic detachment faults generate compression in extension. *Geology*, *45*(10), 923–926. https://doi.org/10.1130/g39232.1

Pickle, R. C., Forsyth, D. W., Harmon, N., Nagle, A. N., & Saal, A. (2009). Thermo-mechanical control of axial topography of intra-transform spreading centers. *Earth and Planetary Science Letters*, *284*(3), 343–351. https://doi.org/10.1016/j.epsl.2009.05.004

Pockalny, R. A. (1997). Evidence of transpression along the Clipperton Transform: Implications for processes of plate boundary reorganization. *Earth and Planetary Science Letters*, *146*(3), 449–464. https://doi.org/10.1016/S0012-821X(96)00253-1

Pockalny, R. A., Fox, P. J., Fornari, D. J., Macdonald, K. C., & Perfit, M. R. (1997). Tectonic reconstruction of the Clipperton and Siqueiros Fracture Zones: Evidence and consequences of plate motion change for the last 3 Myr. *Journal of Geophysical Research*, *102*(B2), 3167–3181. https://doi.org/10.1029/96JB03391

Prigent, C., Warren, J., Kohli, A., & Teyssier, C. (2020). Fracture-mediated deep seawater flow and mantle hydration on oceanic transform faults. *Earth and Planetary Science Letters*, *532*, 115988. https://doi.org/10.1016/j.epsl.2019.115988

Richards-Dinger, K. B., & Shearer, P. M. (2000). Earthquake locations in southern California obtained using source-specific station terms. *Journal of Geophysical Research*, *105*(B5), 10939–10960. https://doi.org/10.1029/2000JB900014

Robinson, D. P. (2011). A rare great earthquake on an oceanic fossil fracture zone. *Geophysical Journal International*, *186*(3), 1121–1134. https://doi.org/10.1111/j.1365-246X.2011.05092.x

Roland, E., Lizarralde, D., McGuire, J. J., & Collins, J. A. (2012). Seismic velocity constraints on the material properties that control earthquake behavior at the Quebrada-Discovery-Gofar transform faults, East Pacific Rise. *Journal of Geophysical Research*, *117*(B11). https://doi.org/10.1029/2012JB009422

Ross, Z. E., Trugman, D. T., Hauksson, E., & Shearer, P. M. (2019). Searching for hidden earthquakes in Southern California. *Science*, *364*(6442), 767–771. https://doi.org/10.1126/science.aaw6888

Schlindwein, V. (2020). Constraining the maximum depth of brittle deformation at slow- and ultraslow-spreading ridges using microseismicity: Comment. *Geology*, *48*(5), e501. https://doi.org/10.1130/G47444C.1

Schlindwein, V., & Schmid, F. (2016). Mid-ocean-ridge seismicity reveals extreme types of ocean lithosphere. *Nature*, *535*(7611), 276–279. https://doi.org/10.1038/nature18277

Searle, R. C. (1983). Multiple, closely spaced transform faults in fast-slipping fracture zones. *Geology*, *11*(10), 607–610. https://doi.org/10.1130/0091-7613(1983)11<607:mcstfi>2.0.co;2

Shi, P., Wei, M. M., & Pockalny, R. A. (2021). The ubiquitous creeping segments on oceanic transform faults. *Geology*. https://doi.org/10.1130/G49562.1

Smith, W. H. F., & Sandwell, D. T. (1997). Global sea floor topography from satellite altimetry and ship depth soundings. *Science*, *277*(5334), 1956–1962. https://doi.org/10.1126/science.277.5334.1956

Tan, Y. J., Tolstoy, M., Waldhauser, F., & Wilcock, W. S. D. (2016). Dynamics of a seafloor-spreading episode at the East Pacific Rise. *Nature*, *540*(7632), 261–265. https://doi.org/10.1038/nature20116

Trugman, D. T., & Shearer, P. M. (2017). GrowClust: A hierarchical clustering algorithm for relative earthquake relocation, with application to the Spanish Springs and Sheldon, Nevada, earthquake sequences. *Seismological Research Letters*, *88*(2A), 379–391. https://doi.org/10.1785/0220160188

Tucholke, B., & Schouten, H. (1988). Kane fracture zone. *Marine Geophysical Researches*, *10*(1–2), 1–39. https://doi.org/10.1007/bf02424659

Van Avendonk, H. J. A., Harding, A. J., Orcutt, J. A., & McClain, J. S. (1998). A two-dimensional tomographic study of the Clipperton transform fault. *Journal of Geophysical Research*, *103*(B8), 17885–17899. https://doi.org/10.1029/98JB00904

Van Avendonk, H. J. A., Harding, A. J., Orcutt, J. A., & McClain, J. S. (2001). Contrast in crustal structure across the Clipperton transform fault from travel time tomography. *Journal of Geophysical Research*, *106*(B6), 10961–10981. https://doi.org/10.1029/2000JB900459

Waldhauser, F., & Ellsworth, W. L. (2000). A double-difference earthquake location algorithm: Method and application to the Northern Hayward Fault, California. *Bulletin of the Seismological Society of America*, *90*(6), 1353–1368. https://doi.org/10.1785/0120000006

Wang, R., Schmandt, B., Zhang, M., Glasgow, M., Kiser, E., Rysanek, S., & Stairs, R. (2020). Injection-induced earthquakes on complex fault zones of the Raton basin illuminated by machine-learning phase picker and dense nodal array. *Geophysical Research Letters*, *47*(14), e2020GL088168. https://doi.org/10.1029/2020GL088168

Wolfson-Schwehr, M., & Boettcher, M. S. (2019). Global characteristics of oceanic transform fault structure and seismicity. In J. C. Duarte (Ed.), *Transform plate boundaries and fracture zones* (pp. 21–59). Amsterdam: Elsevier. https://doi.org/10.1016/b978-0-12-812064-4.00002-5

Wolfson-Schwehr, M., Boettcher, M. S., & Behn, M. D. (2017). Thermal segmentation of mid-ocean ridge-transform faults. *Geochemistry, Geophysics, Geosystems*, *18*(9), 3405–3418. https://doi.org/10.1002/2017GC006967

Wolfson-Schwehr, M., Boettcher, M. S., McGuire, J. J., & Collins, J. A. (2014). The relationship between seismicity and fault structure on the Discovery transform fault, East Pacific Rise. *Geochemistry, Geophysics, Geosystems*, *15*(9), 3698–3712. https://doi.org/10.1002/2014GC005445

Yu, Z., Singh, S. C., Gregory, E. P. M., Maia, M., Wang, Z., & Brunelli, D. (2021). Semibrittle seismic deformation in high-temperature mantle mylonite shear zone along the romanche transform fault. *Science Advances*, *7*(15), eabf3388. https://doi.org/10.1126/sciadv.abf3388

Zhang, H., & Thurber, C. H. (2003). Double-difference tomography: The method and its application to the Hayward fault, California. *Bulletin of the Seismological Society of America*, *93*(5), 1875–1889. https://doi.org/10.1785/0120020190

Zhang, M., Ellsworth, W. L., & Beroza, G. C. (2019). Rapid earthquake association and location. *Seismological Research Letters*, *90*(6), 2276–2284. https://doi.org/10.1785/0220190052